SUPPORTING INFORMATION

One-step flashlight processing of MOF thin films for non-linear light absorption

Nikolaj A. Zhestkij,[*a] Svyatoslav A. Povarov,[a] Lev Volodin,[b] Rostislav Chelmodeev,[b] Mikhail Melkomukov,[b] Yulia Kenzhebayeva,[a] Sergey S. Rzhevskiy,[a] Sergei A. Shipilovskih,[a] Anastasia V. Lubimova,[a] Maria V. Timofeeva,[a] Valentin A. Milichko[*c]

[a.] School of Physics and Engineering, ITMO University, St. Petersburg, 197101, Russia.

[b.] Faculty of Power Engineering, Bauman Moscow State Technical University, Moscow, 105005 Russia.

[c.] Institut Jean Lamour, Universite de Lorraine, UMR CNRS 7198, 54011 Nancy, France.

[*] E-mail: valentin.milichko@univ-lorraine.fr; nikolaj.zhestkij@metalab.ifmo.ru

Part 1. HKUST-1

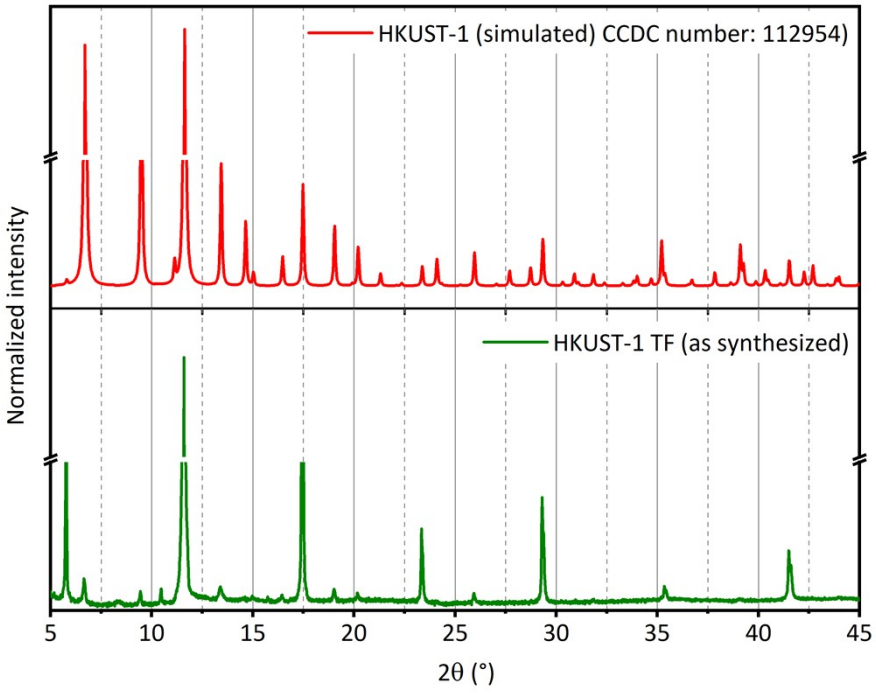

Fig. S1. PXRD spectra of simulated HKUST-1 (CCDC number: 112954; red curve) and synthesised HKUST-1 TF (green curve).

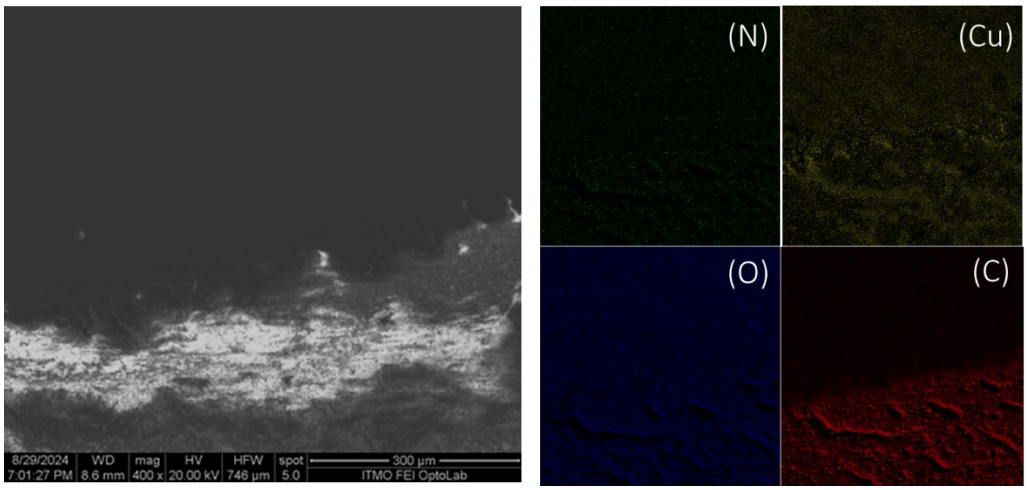

Fig. S2. EDS mapping of HKUST-1 TF illustrating the uniformity of elements distribution and the border between the exposed and initial areas of HKUST-1TF.

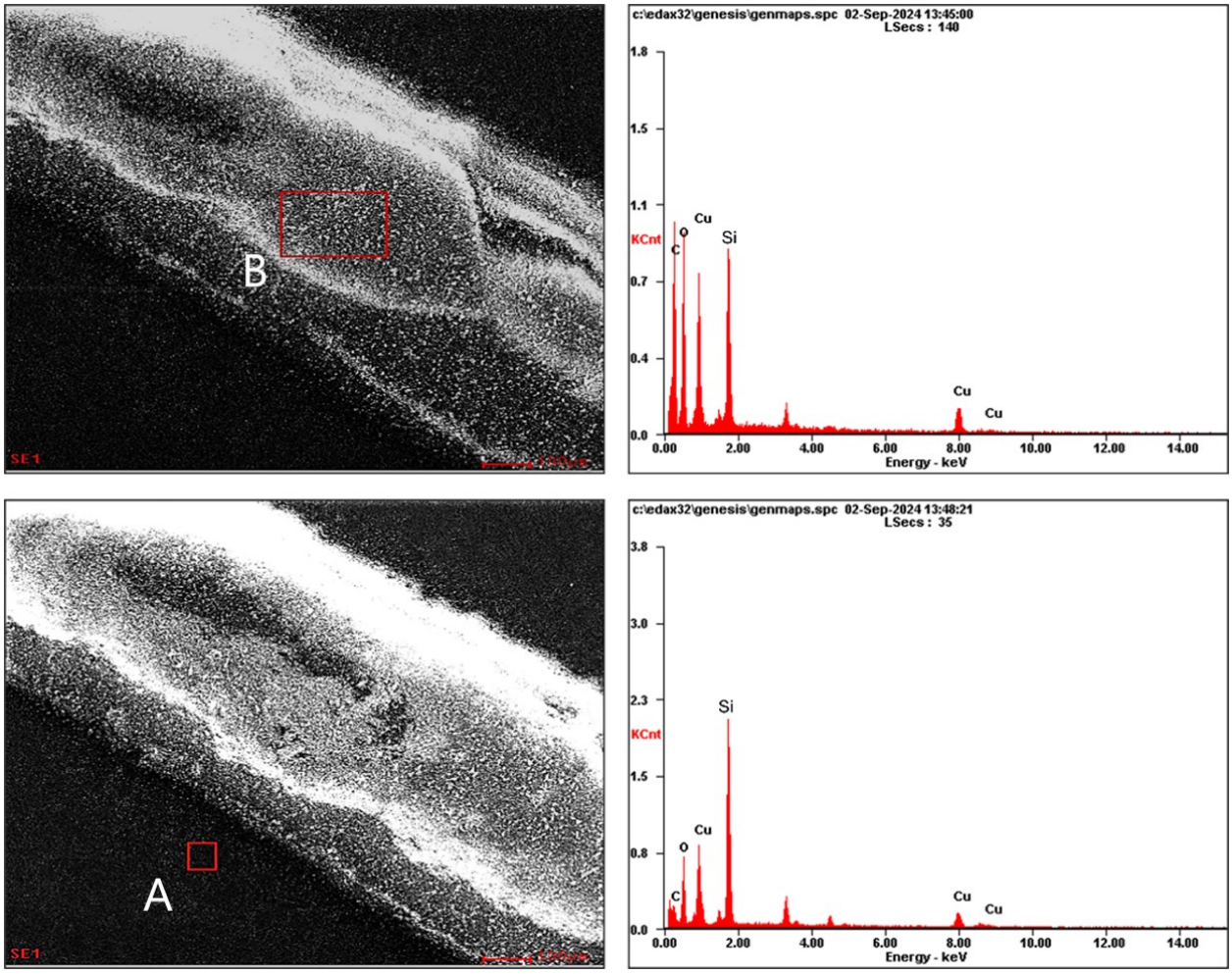

Fig. S3. EDX spectra of the initial (A) and exposed (B) areas of HKUST-1 TF, confirming the carbon evaporation from the surface during the flashlight patterning (see also optical image in Fig. S19).

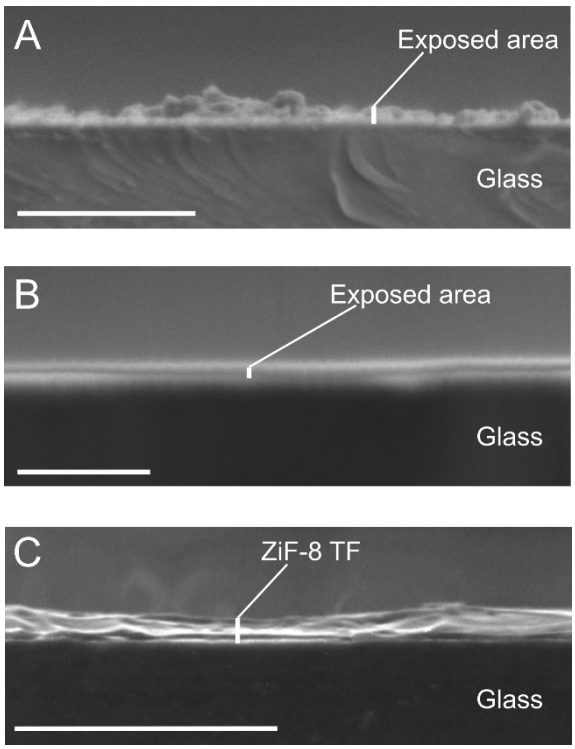

Fig. S4. The cross-section SEM micrographs illustrating the thikness of the exposed areas: (A) The exposed HKUST-1 TF (logo «Faculty of Physics» pattern from the Fig. 1B), (B) ZIF-8 TF exposed area and (C) ZIF-8 TF masked area. Scale bars: 500 nm (A,B), 10 μm (C).

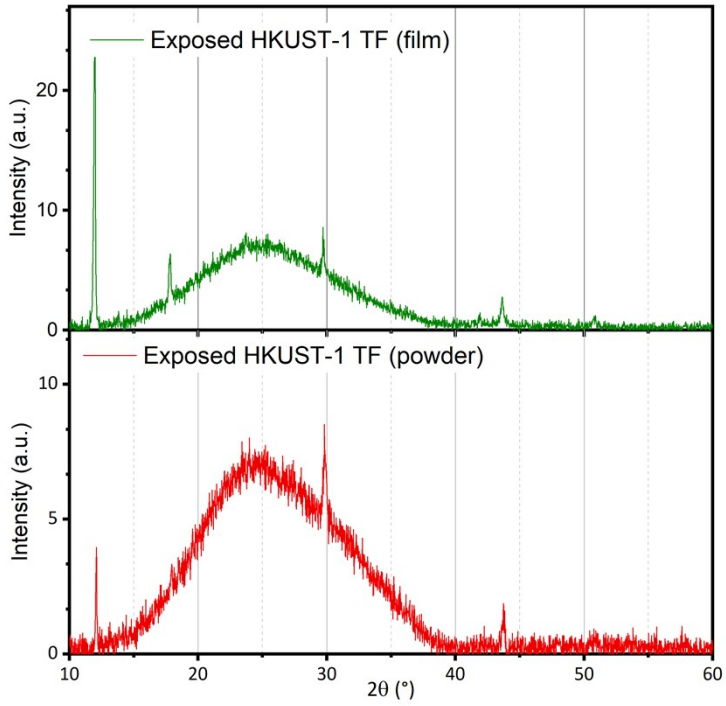

Fig. S5. PXRD spectra of HKUST-1 TF after flashlight processing: the data obtained from the TF on the glass substrate (green curve) and the powder removed (scratched off) from this substrate (red curve).

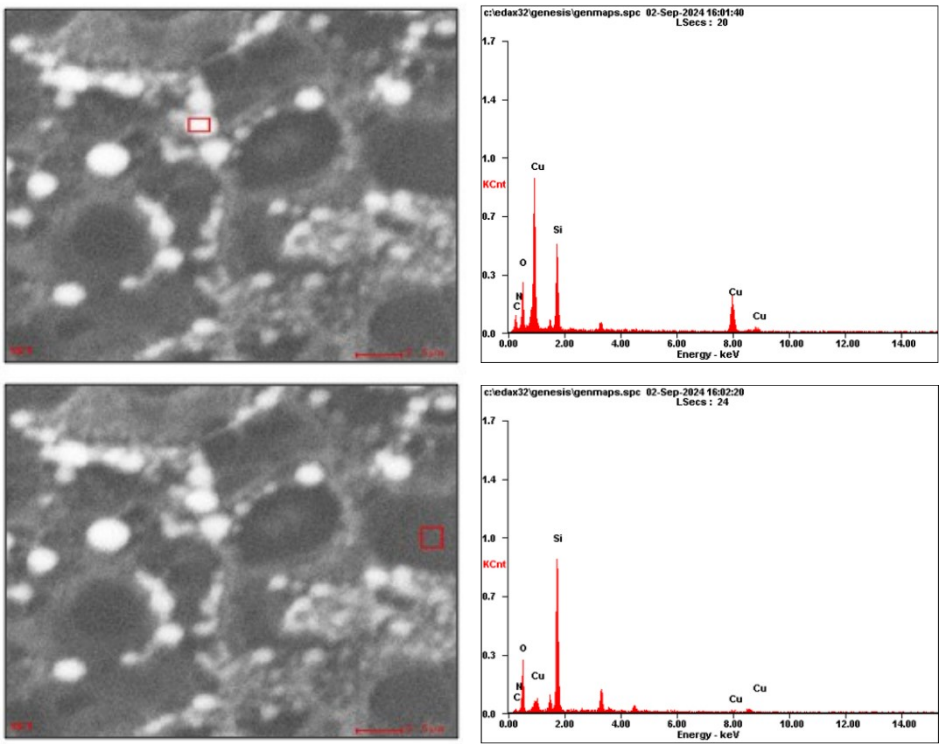

Fig. S6. The EDS spectra of different areas of the HKUST-1 TF after flashlight patterning.

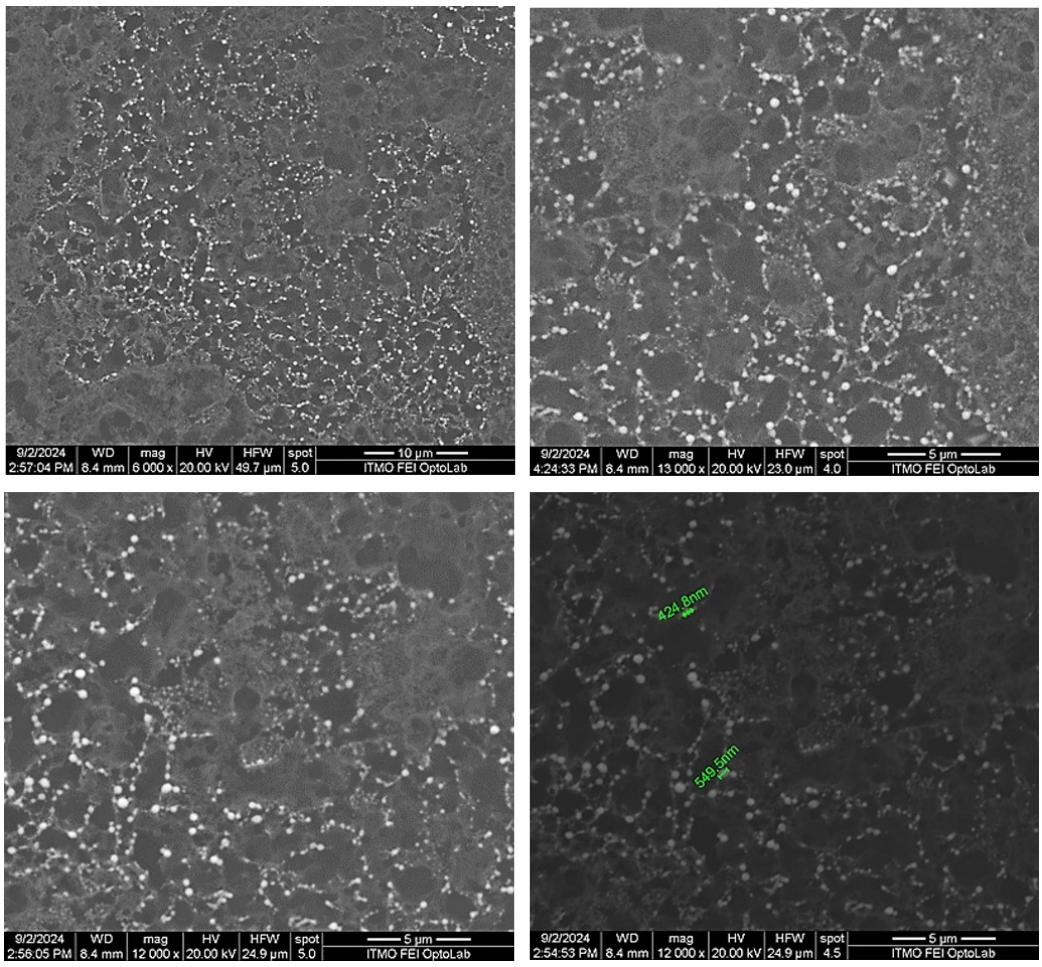

Fig. S7. SEM micrographs of various areas of HKUST-1 TF after flashlight patterning, illustrating the agglomerates of copper particles inside an amorphous carbon matrix.

Part 2. Bimetallic HKUST-1

Synthesis of HKUST-1 (Cu-Ni).

A mixture of 36 mg of $CuSO_4*5H_2O$ (0.144 mmol), 41 mg of $NiSO_4*7H_2O$ (0.144 mmol), and 60 mg of 1,3,5-benzenetricarboxylic acid (0.286 mmol) was dissolved in 3 mL of a solvent mixture (EtOH/DMF/$5H_2O$ – 1/1/1) under ultrasound (25 min). After the solution mixture was placed into 4 ml vial and hermetically sealed with a lid with a rubber septum to exclude the interaction with the external environment and create excess pressure in the vessel. The solution mixture was heated to 85 °C and kept for 24 hours. After 24 hours the reaction mixture was cooled down to room temperature. The resulting crystals of HKUST-1 (Cu-Ni) were separated from the mother liquid by filtration, then it was repeatedly washed 5 times with mixture of DMF/H_2O/EtOH. The washed crystals were dried in the air. Pale blue crystals of HKUST-1 (Cu-Ni) were obtained.

Synthesis of HKUST-1 (Cu-Co).

A mixture of 36 mg of $CuSO_4*5H_2O$ (0.144 mmol), 41 mg of $CoSO_4*7H_2O$ (0.144 mmol), and 60 mg of 1,3,5-benzenetricarboxylic acid (0.286 mmol) was dissolved in 3 mL of a solvent mixture (EtOH/DMF/$5H_2O$ – 1/1/1) under ultrasound (25 min). After the solution mixture was placed into 4 ml vial and hermetically sealed with a lid with a rubber septum to exclude the interaction with the external environment and create excess pressure in the vessel. The solution mixture was heated to 85 °C and kept for 24 hours. After 24 hours the reaction mixture was cooled down to room temperature. The resulting crystals of *HKUST-1 (Cu-Co)* were separated from the mother liquid by filtration, then it was repeatedly washed 5 times with mixture of DMF/H_2O/EtOH. The washed crystals were dried in the air. Blue crystals of *HKUST-1 (Cu-Co)* were obtained.

Synthesis of HKUST-1 (Cu-Fe).

A mixture of 36 mg of $CuSO_4*5H_2O$ (0.144 mmol), 40 mg of $FeSO_4*7H_2O$ (0.144 mmol), and 60 mg of 1,3,5-benzenetricarboxylic acid (0.286 mmol) was dissolved in 3 mL of a solvent mixture (EtOH/DMF/$5H_2O$ – 1/1/1) under ultrasound (25 min). After the solution mixture was placed into 4 ml vial and hermetically sealed with a lid with a rubber septum to exclude the interaction with the external environment and create excess pressure in the vessel. The solution mixture was heated to 85 °C and kept for 24 hours. After 24 hours the reaction mixture was cooled down to room temperature. The resulting crystals of *HKUST-1 (Cu-Fe)* were separated from the mother liquid by filtration, then it was repeatedly washed 5 times with mixture of DMF/H_2O/EtOH. The washed crystals were dried in the air. Green crystals of *HKUST-1 (Cu-Fe)* were obtained.

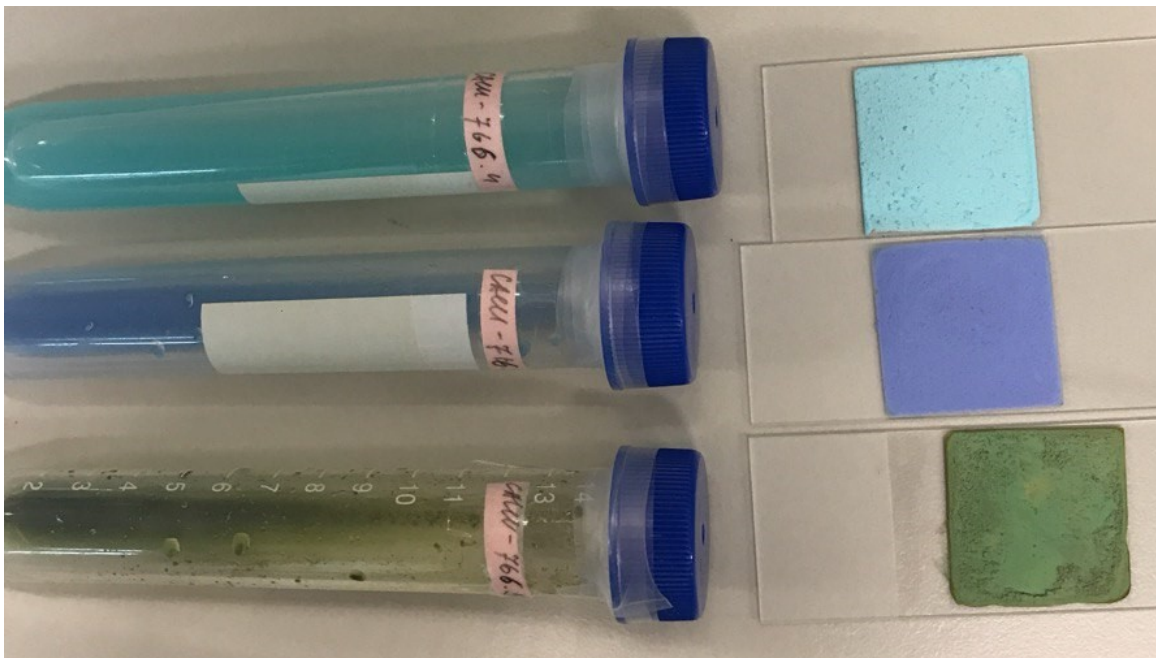

Fig. S8 Bimetallic MOFs based on HKUST-1: pale blue (Cu-Ni), blue (Cu-Co), and green (Fe-Cu) in solution (left). The glass covered with the corresponding bimetallic MOFs (right).

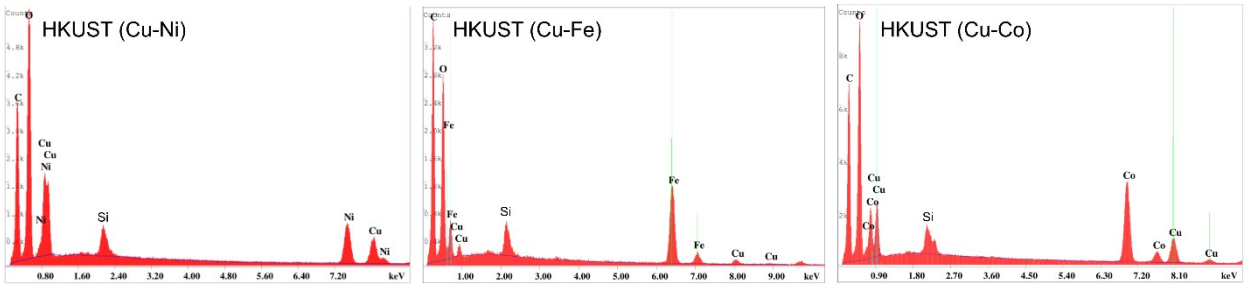

Fig. S9. The EDS spectra of bimetallic MOFs based on HKUST-1.

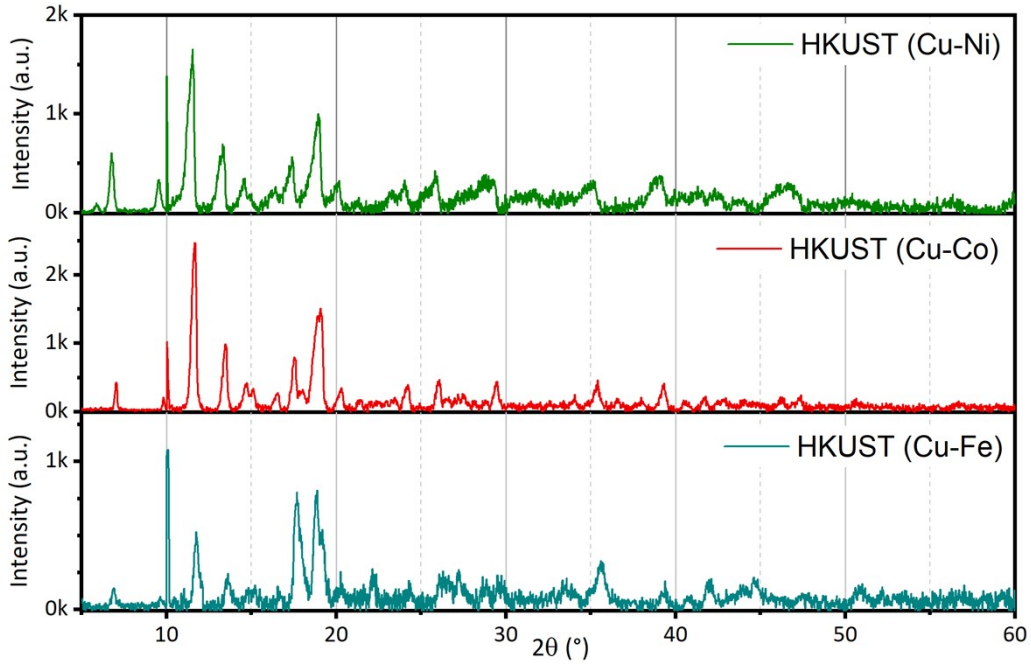

Fig. S10. The PXRD spectra of bimetallic MOFs based on HKUST-1.

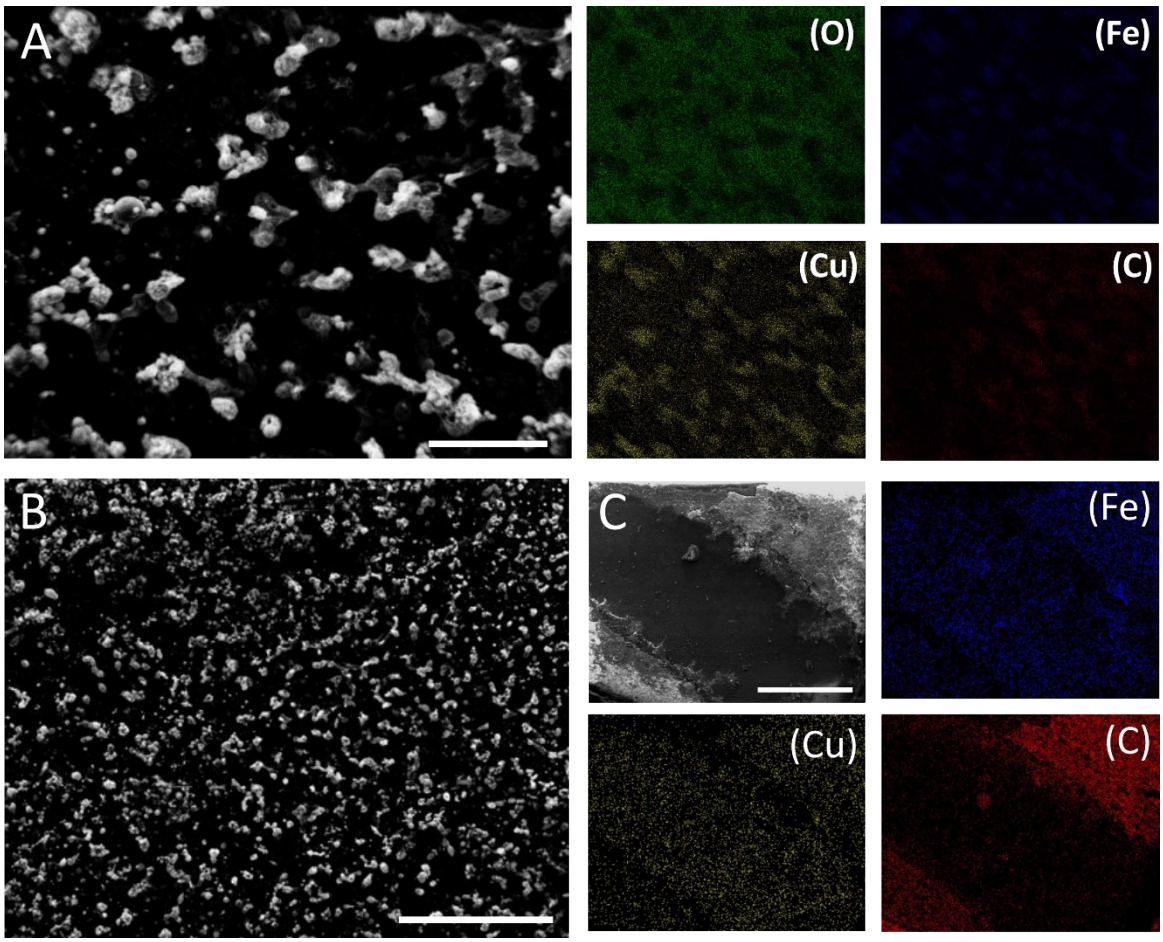

Fig. S11. (A) SEM micrograph and the corresponding EDS map of HKUST-1 TF (Cu-Fe) after flashlight processing. Scale bar, 10 μm. (B) SEM micrograph of HKUST-1 TF (Cu-Fe) after flashlight processing. Scale bar, 50 μm. (C) The SEM micrograph and the EDS map of the exposed (diagonal line) and masked (sides) areas of HKUST-1 TF (Cu-Fe). Scale bar, 1 mm.

Part 3. ZIF-8

ZIF-8 films were prepared by spin coating using a drop-casting method with alternating deposition of zinc acetate and 2-methylimidazole solutions onto glass substrates. The substrates were cleaned sequentially in deionized water and ethanol for 10 minutes each in an ultrasonic bath, followed by 15 minutes of UV treatment to enhance adhesion. A 10 mM solution of 2-methylimidazole in 50 mL isopropanol and a 20 mM solution of zinc acetate in 50 mL isopropanol were prepared and sonicated for 20 minutes prior to deposition. The deposition was performed using a self-made automatic spincoater setup, with the table preheated to 40°C. The spin speed was set to 1500 rpm, and the deposition cycle was repeated 1500 times to achieve the desired film thickness. After spin coating, the films were dried at room temperature for 15 minutes.

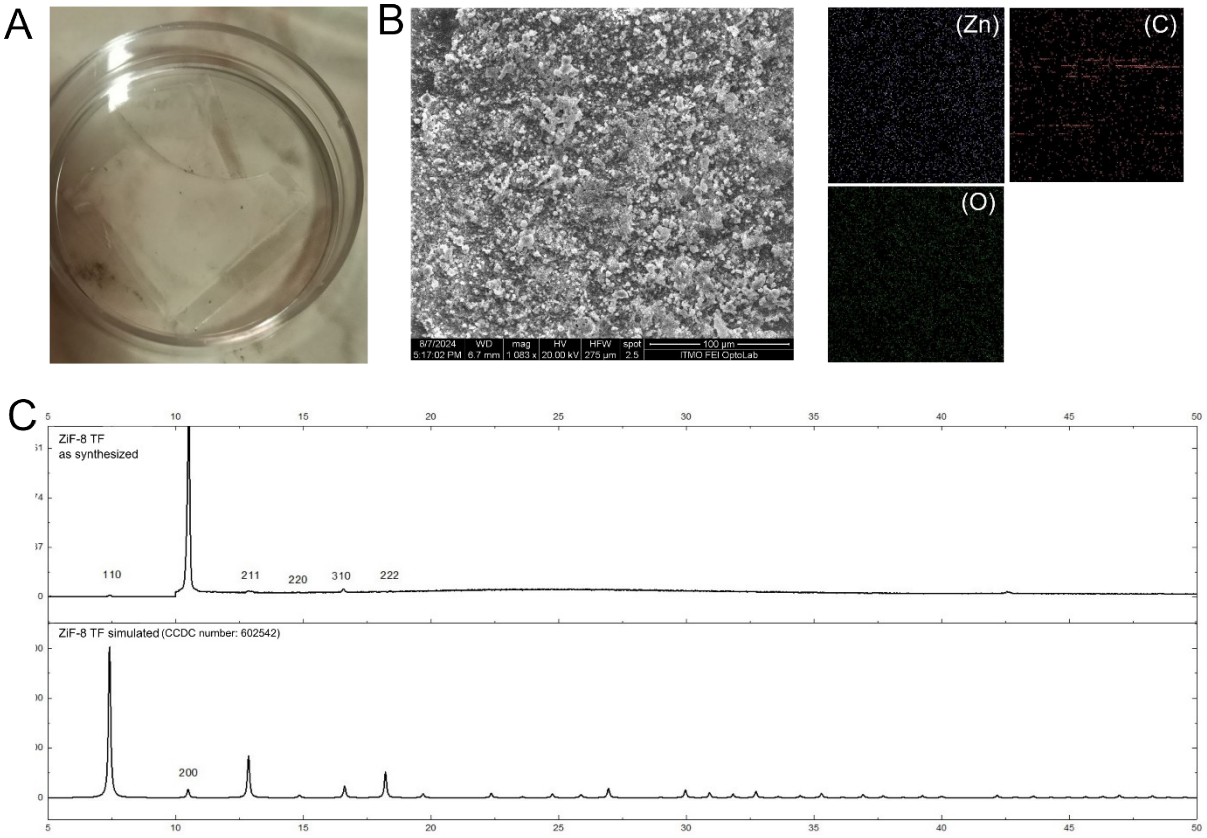

Fig. S12. (A) An optical image of the as-synthesized ZIF-8 TF with corresponding EDS map (B) and PXRD spectra (C, simulated pattern: CCDC 603542).

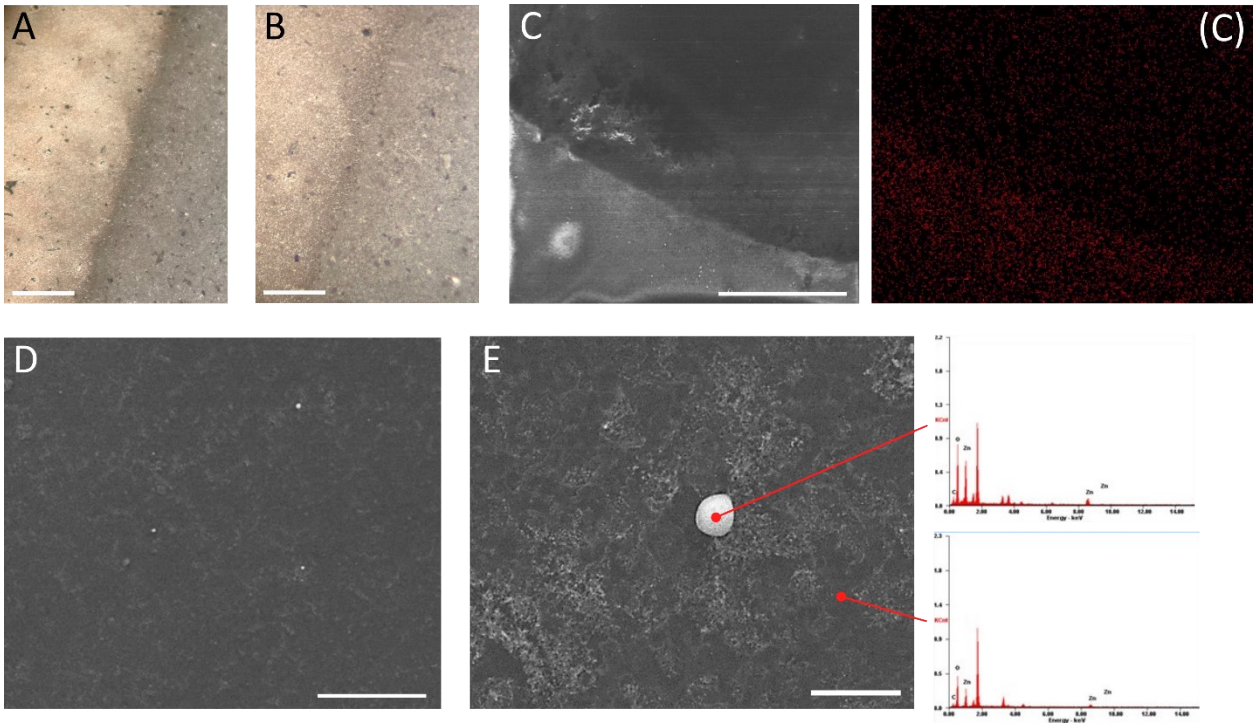

Fig. S13. (A, B) Optical images of patterned (left) and masked (right) areas of ZIF-8 TF. Scale bars, 200 μm (A), 100 μm (B). (C) SEM micrograph of border between patterned and masked areas of ZIF-8 TF and the corresponding EDS map of carbon distribution. Scale bar, 1mm. (D) SEM mocrograph of ZIF-8 TF patterned area. Scale bar, 50 μm. (E) SEM micrograph and the EDS spectra of the Zn-agglomerated particle. Scale bar, 5 μm.

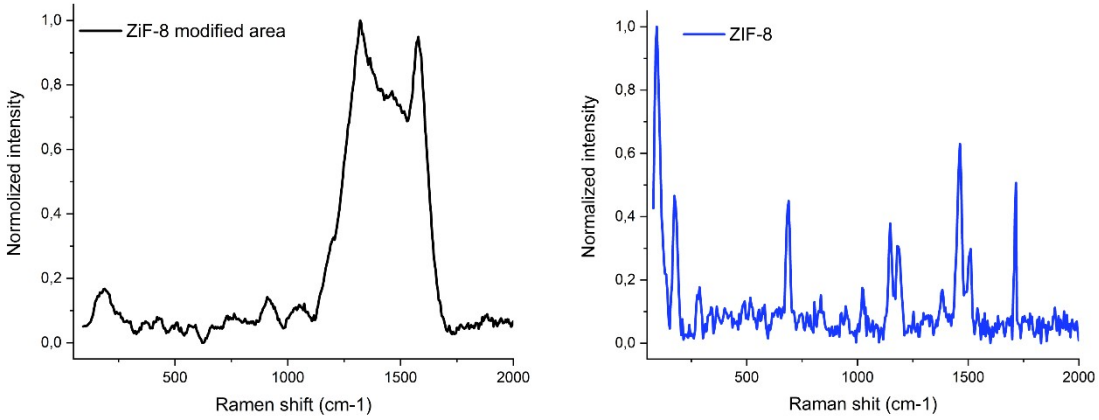

Fig. S14. Raman spectra of the exposed (left) and initial (right) areas of ZIF-8 TF.

Part 4. The flashlight optical setup

The experimental setup consists of irradiation module and a lamp ignition and charging system. To determine the optical characteristics of pulse, it is necessary to calculate the corresponding parameters of the discharge circuit. The radiation dose directly depends on the electrical energy invested in the arc discharge of the xenon lamp. Consider the power and ignition scheme, figure S3.

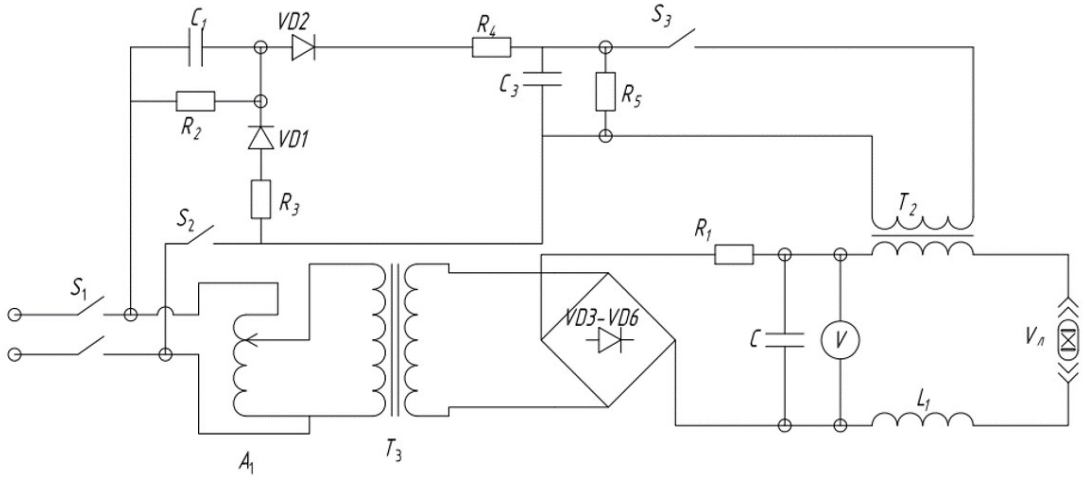

Fig. S15. The electric scheme of the flashlight irradiation setup.

The discharge circuit is represented by a capacitor C = 200 uF, connecting wires with inductance L1, a secondary winding of a pulse transformer T2 (a toroidal transformer on a ferrite core) and a pulsed xenon lamp IFP 800. The key parameters of the system are following:

1. U_0 = 700-1800 V – Voltage;
2. p_0 = 400 Torr – Initial xenon pressure;
3. C = 200 uF – Condensor capacity;
4. L = 80 mm – distance between electrodes;
5. d = 7 mm – inner lamp diameter;
6. L = 21 uH – Circuit induction;
7. R_0 = 190 mOhm – Circuit resistance;

The capacitive storage device is charged from a high voltage source 2, consisting of a laboratory auto-transformer (LATR) A1, powered by a 230 V, 50 Hz network; a high-voltage transformer T_3, a diode bridge consisting of high-voltage diodes VD3-VD6 and a current-limiting resistor R_1.

Charging of the capacitive storage device is carried out as follows:

1) When the key S_1 is closed (the unit is switched on), the main voltage is applied to LATR A_1.

2) The output alternating voltage from LATR – from 0 to 200 V (50 Hz) (determined by the angle of rotation of the adjusting knob-regulator) is supplied to the primary winding of the high-voltage transformer T_3 (transformation coefficient ~ 20).

3) The increased alternating voltage is rectified by the diode bridge VD_3-VD_6.

4) Charging of the capacitive storage is carried out through a current-limiting resistor R_1 (~100 kOhm)

5) The ignition of the pulse lamp is realized according to the sequential ignition scheme by circuit 3.

Charging of the ignition capacitor C_3 (~ 1 uF), included in the circuit with the primary winding of the pulse transformer T_2, occurs according to the doubling scheme (U ~ 650V). Ignition initiation occurs when the S_3 key (thyristor key) is closed. When the capacitor C_3 is discharged onto the primary winding of the pulse transformer T_2, a high-frequency high-voltage voltage pulse with an amplitude (~ 30 kV) is generated on the secondary winding T_2 in the power circuit 1, sufficient for the breakdown of the interelectrode gap in the lamp. The key parameters of the discharge circuit were preliminarily calculated for several irradiation regimes in order to evaluate the efficiency of converting accumulated electrical energy into radiation. The data representing the calculated contour parameters is given in Table S1.

Table S1. Discharge circuit parameter for various regimes of irradiation.

Charge voltage (kV)	0.7	1.0	1.4	1.8
Accumulating energy (J)	49	100	196	324
Current max (A)	724	1158	1775	2420
Equivalent lamp resistance (mOhm)	527	417	336	288
Current maximum duration (us)	724	72.7	74.8	76.1
Discharge duration on FWHM	527	145.3	143.3	142.2
Electric power max (MW)	0.28	0.56	1.06	1.69
Energy conversion efficiency	73.5%	68.7%	63.9%	60.3%
Circuit attenuation parameter	1.086	0.924	0.806	0.733

The shape and dimensions of the reflector are largely decisive, to assess the uniformity of the field distribution, the reflector was modeled in the TracePro software package. The irradiator, in its simplified form, consists of two parts: a radiation source (lamp) and a reflector. Since the properties of the radiation source are not considered in this case, for simplicity of calculation, the lamp was assigned a luminous flux each mount of accumulated energy. The lamp is simplistically represented by a cylinder equal in size to the body of the glow, a model of a surface radiation source with a Lambert angular distribution was adopted. The ability of the plasma in the lamp to emit in a wide range of wavelengths and the similarity with the blackbody model were not taken into account in this calculation. For the reflector, a material with a good mirror reflection "Ar mirror" was selected from the program catalog. The results of modeling the irradiance field are shown in Fig. S16. It is clearly seen that at the location of the sample, the uniformity of the field distribution is close to the ideal.

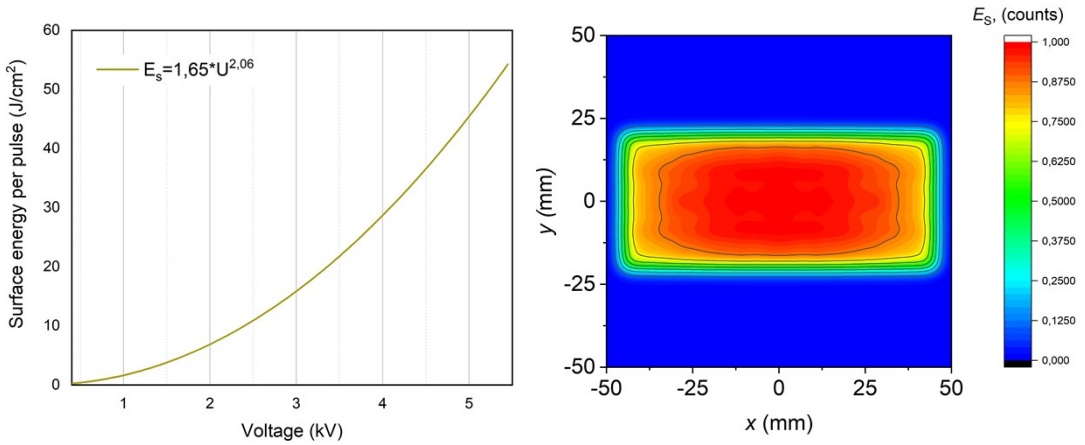

Fig. S16. (Left) The estimation of surface energy irradiation depending on the discharge voltage; (Right) The simulation of irradiance field distribution for the utilized configuration of reflector.

Table S2. Irradiation data for Fig. S16.

U, kV	**Calc. Energy, J cm^{-2}**	**Measured. Energy, J cm^{-2}**	**Error, J cm^{-2}**
0,5	0,40	0,17	0,003
0,7	0,79	0,29	0,008
1	1,62	0,52	0,002
1,4	3,36	0,83	0,004
1,8	5,54	1,31	0,003

The radiation energy density values in the reflector output window for various regimes were determined by a pyroelectric detector PEM 8 (SLT Sensor & Lasertechnik GmbH, Wildau, Germany) with a stainless-steel mesh attenuating the radiation flux (transmission ~ 5%). The obtained values were approximated to determine the energy density for intermediate values of charging voltages (Fig. S16, left). Additional studies using photodetectors have shown that the characteristic duration of the radiation pulse coincides with the duration of the discharge current. This made it possible to estimate the values of the radiation power density in the output window of the reflector.

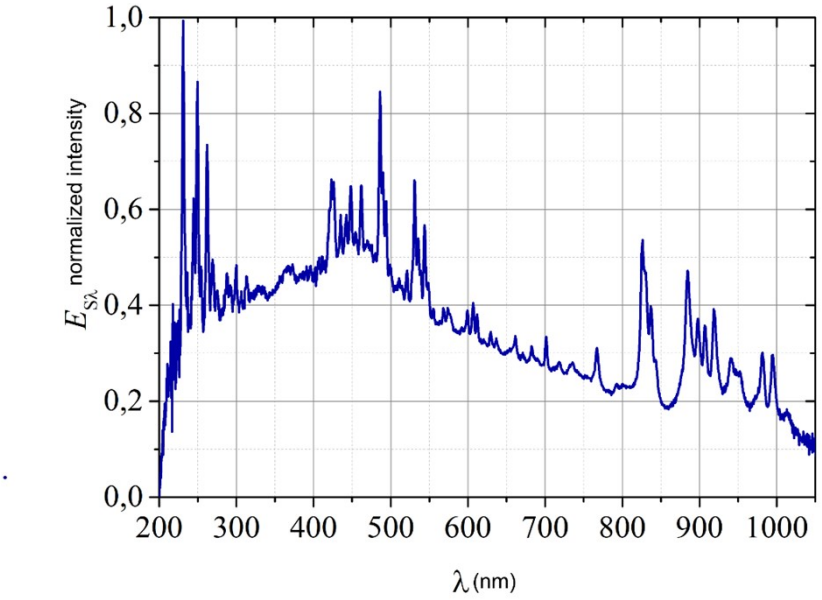

Fig. S17. Measured spectra of the pulsed Xenon lamp, utilized as a light source in flashlight sintering.

Based on the simulation data, it can be concluded that the losses associated with the delivery of radiation energy to the sample are negligible and do not make a significant contribution to the experiment. Thus, an empirical formula that takes into account only the internal parameters of the contour can be used to calculate the radiation dose.

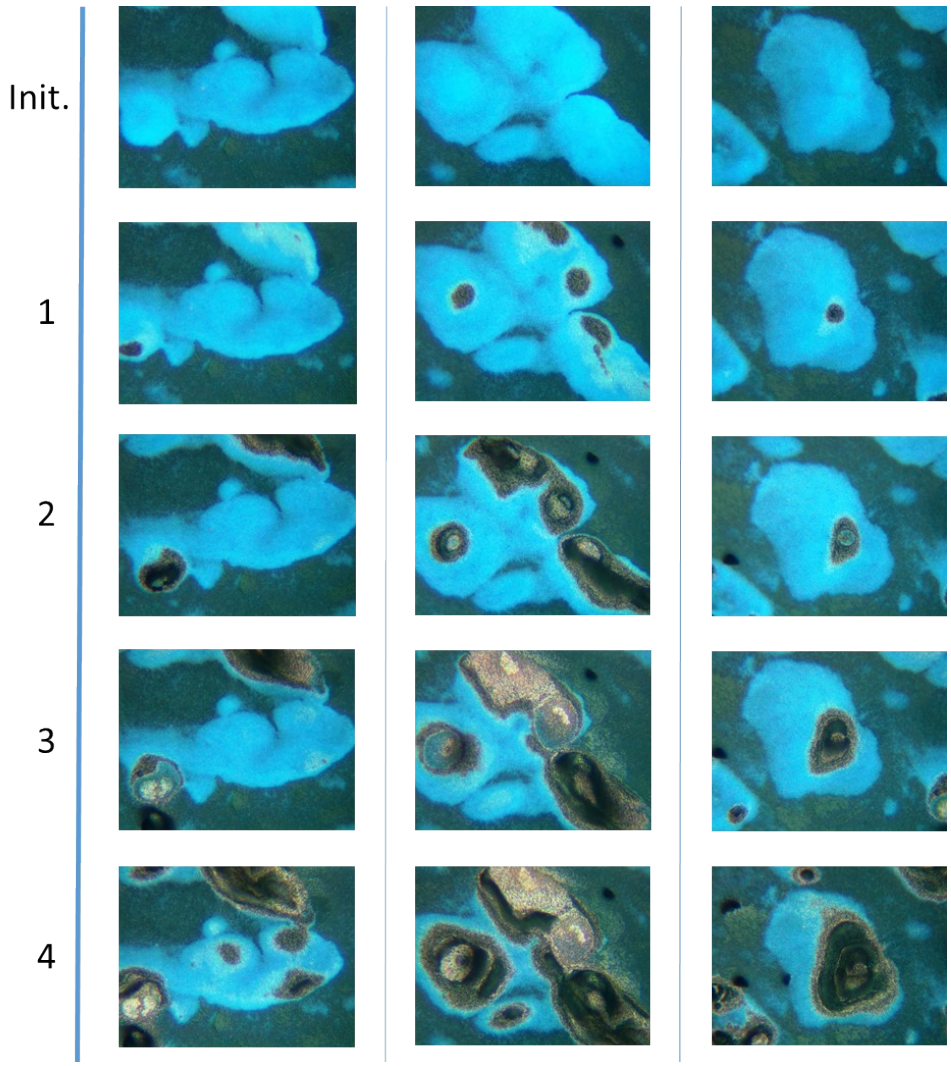

Fig. S18. Microscopic image demonstrating of pulse-by-pulse changes in HKUST-1 TF after the series of four pulses with the surface energy value of 1.8 J/cm^2

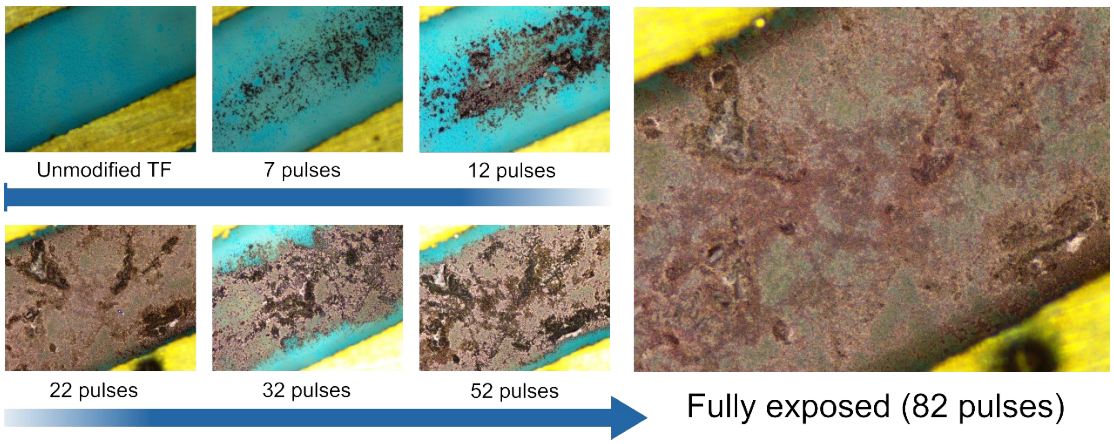

Fig. S19. Microscopic image demonstrating of pulse-by-pulse changes in HKUST-1 TF after the series of 7 to 82 pulses with the surface energy value of 1.8 J/cm^2

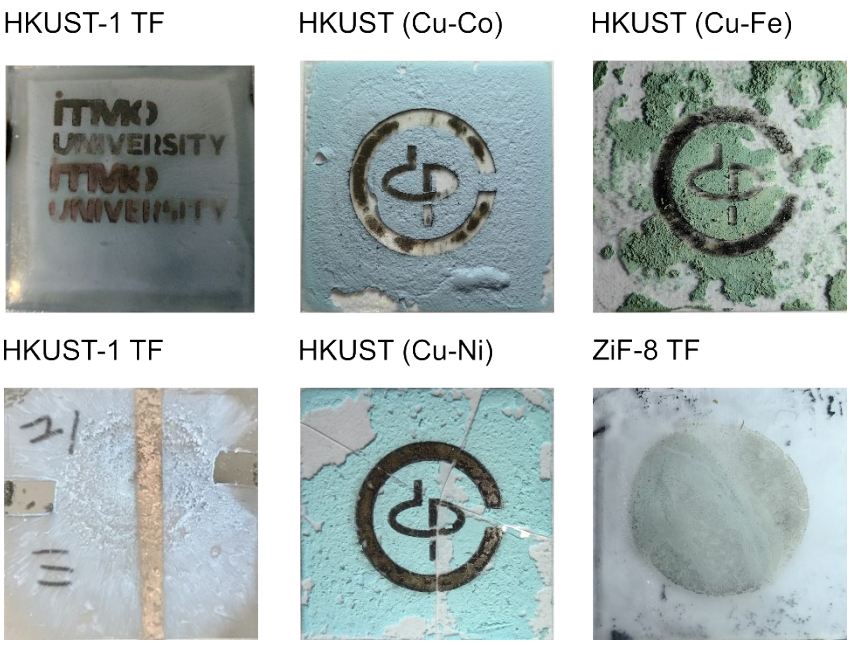

Fig. S20. Optical images of various MOF's TFs after the flashlight processing.

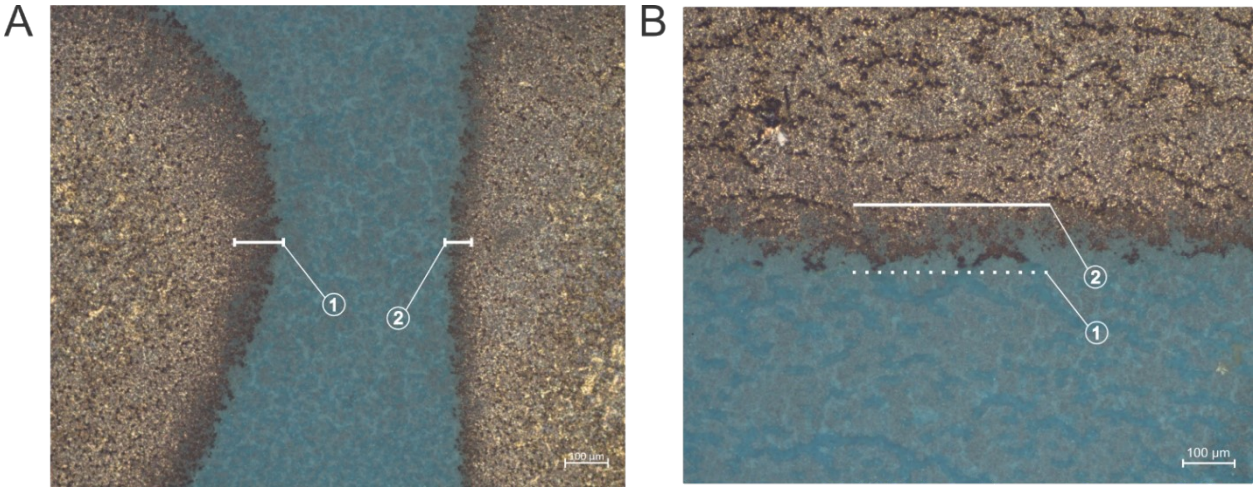

Fig. S21. The selected regions from "arbitrary pattern" (Fig. 1D) indicating the flashlight processing heat distribution driven resolution: (A) The stripe and circle edges (R = 1 mm element size) with 120 µm and 70 µm heat inhomogeneity areas and the stripe edge (B) with 100 µm (R = 0.75).

Table S3. Overview of non-optical approaches of top-down MOF patterning.

Approach	Source	Resolution	Speed / Exposure time	MOF	Product of patterning	Substrate	Ref
X-Ray photolithography	Synchrotrone radiation	50 nm	3 min at a ring energy of 2 GeV	ZIF-71, ZIF-71-Co, ZIF-72 and ZIF-8	Structures from initial MOF with the same composition	Silicon wafer (Si-MAT) with preparation for film deposition (ALD, etching)	[25]
Resist-free X-Ray photolithography		10 µm	40 s at 1748 J cm^{-2} X-ray dose	$Cu_2[(Br_2BDC)_x(BDC)_{1-x}]_2DABCO$ (x = Br_2BDC/(BDC + Br_2BDC)		Silicon wafer with $Cu(OH)_2$ nanobelts deposed	[27]
e-beam patterning	Thermo Fisher Helios G4 UC Focused Ion Dual Beam microscope	30 - 400 nm	1 µs	ZIF-8		Silicon wafer with pre-deposed layer of ZIF liquid solution	[77]
Direct photo- and e-beam lithography	ThermoFisher Helios G4 UC Focused Ion Dual Beam microscope (5 kV); UV light source (254 nm), low-pressure mercury vapor grid lamp	70 nm / 5 µm		ZIF-8, ZIF-7, HKUST-1, UiO-66, Eu-BTC		Crystalline quarts, ITO	[26]
Electrochemical lithography		200-250 µm		UiO-66, MIL-96	Structures from MOF microcrystals with metal deposed on the top	Au-covered silicon wafer	[78]
Chemical etching	Etching in HCl	mm scale	> 2h	MIL-88A	MOF films with gradient thickness	PVDF	[79]
Direct crack patterning		–	> 30 min	ZIF-8	MOF films with cracks of controllable thickness	Silicon wafer, flexible plastics, and Al	[80]

Part 5. Z-scan analysis

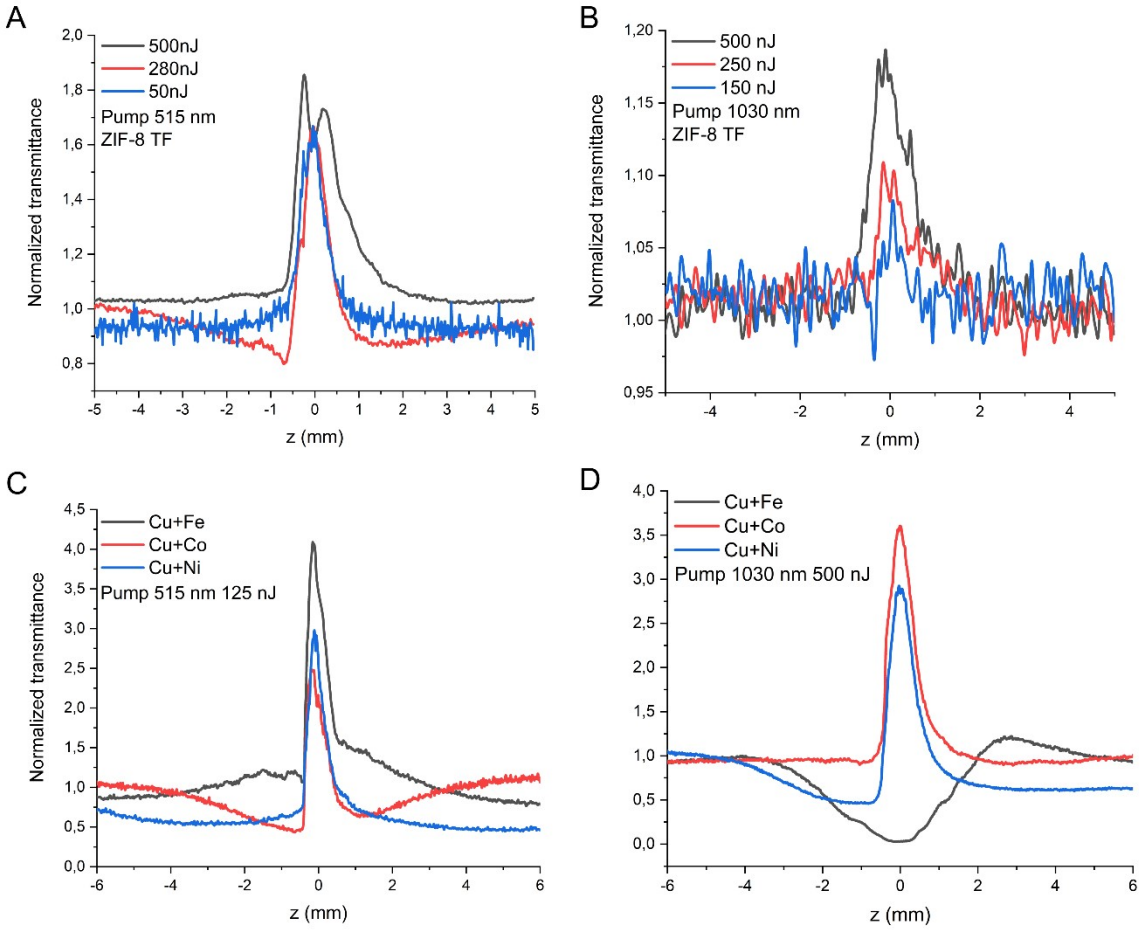

Fig. S22. Z-scan curves for the patterns on ZIF-8 (A-B) and bimetallic HKUST-1 (C-D) TFs after the flashlight processing.

Z-scan analysis:

For z-scan, two key parameters, β_{eff} and I_{sat}, describe the physical phenomena of nonlinear absorption and saturable absorption (SA) of light. These two parameters affect the shape of the transmission curve T(z) in Fig. 5, S22, which is calculated using the following formula:[40,41]

$$T(z) = 1 - \frac{\beta_{eff} I_0 L_{eff}}{2\sqrt{2}} \frac{1}{1 + (\frac{z}{z_R})^2} \frac{1}{1 + \frac{I_0}{I_{sat}} \cdot \frac{1}{1 + (\frac{z}{z_R})^2}}$$

, where:

where β_{eff} is the effective nonlinear absorption coefficient (in cm/GW), and I_{sat} is the saturation intensity (in GW/cm²), I_0 means the peak intensity of the laser beam at a focus ($I_0 = \frac{P}{\pi r_0^2}$). $P = \frac{E}{\tau}$, where E is a laser energy, τ is a laser pulse duration, and ω_0 is a laser beam focus point radius:

$$\omega_0 = \frac{4\lambda f}{\pi D},$$

where D –is a laser beam diameter, f is a lens focal length. The Rayleigh length is $z_R = \frac{\pi {\omega_0}^2}{\lambda}$.

L_{eff} represents the effective absorption length of the sample, and can be defined as:

$$L_{eff} = \frac{(1 - e^{-\alpha L})}{\alpha},$$

where α is a linear absorption coefficient of the sample, and L is a sample thickness.

Calculation parameters

To calculate the parameter β_{eff} for the patterns on MOFs TFs, using the specified formula, the following parameters were used (for ZIF-8): laser pulse energy of 50 nJ, laser pulse duration of 270 fs, lens focal length of 50 mm, laser beam diameter of 3 mm, sample thickness of 50 nm (Fig. S4), linear absorption coefficient α_0 of 2.94×10^5 cm^{-1}, laser beam radius at focus ω_0 of ~10.93 μm, and I_{sat} of ~34.3 GW/cm². For HKUST-1: laser pulse energy of 97 nJ, laser pulse duration of 270 fs, objective focal length of 20 mm, laser beam diameter of 8.3 um, sample thickness of 100 nm (Fig. S4), linear absorption coefficient α_0 of 1.47×10^5 cm^{-1}, and I_{sat} of ~16.04 GW/cm².

Table S4. List of optical limiting materials (metals, MOFs, and polymers). SA, saturation absorption; RSA, reverse saturation absorption.

Sample	**Wavelenght, nm**	**β_{eff}, cm GW^{-1}**	**Process**	**Ref.**
Patterned HKUST-1 TF	515	-5.11×10^2	SA	This work
	1030	-1.172×10^4		
Patterned ZiF-8 TF	515	-1.681×10^3	SA	This work
	1030	-1.624×10^2		
Metals and semiconductors				
50Å Au film	532	5.3×10^6	RSA	[59]
Au film	630 (0.1 ps)	$6{,}8\times10^2$	RSA	[60]
	630 (5.8 ps)	$6{,}7\times10^4$		

NF-RGO	532	0.28×10^{2}	RSA	[61]
NF-RGO/AgNPs (1 M)		1.39×10^{2}		
CdSe (3.54nm)	532	-85	SA	[62]
CdSe:Au (3.54 nm, conc. ratio 1/2.5)		-290		
Cu: $SrTiO_3$ ($D = 1 \times 10^{16}$ ion/cm^2, $t < 1$ ps)	775	1.78×10^{-3}	RSA	[63]
Cu: $SrTiO_3$ ($D = 5 \times 10^{16}$ ion/cm^2, $t = 2.46$ ps)		4.23×10^{-3}		
MOFs, polymers, and carbon				
$[Cd(imz)_3]_2(BTC)\cdot0.5H_2O$	532	5.45	RSA	[64]
$[Cu_4(H_2O)_2(imz)_8](BTC)_2\cdot7H_2O$		9.81		
AZO	1064	460	RSA	[65]
P_2Pt	532	50	RSA	[66]
	1064	10		
PMOF-2/PDMS	532	1.17×10^{3}	RSA	[67]
Co-TCPP(Fe) MOF nanosheets	532	42.35	RSA	[68]
Mg-MOF-74	1080	-1×10^{9}	SA, RSA	[53]
	1940	-4.38×10^{9}		
	2850	-6.8×10^{9}	SA	

ZnTPyP-1(Zn/Cu)/PDMS	532	4.65×10^{3}	RSA	[69]
TPyP(Cu)/PDMS		40		
ZnTPyP(Cu) film	532	$\sim5.7\times10^{5}$	RSA	[52]
ZnTPyP(H2) film		$\sim5.1\times10^{4}$		
InTCPP($Fe^{3+}Cl^{-}$)	532	$\sim6.35\times10^{5}$	RSA	[70]
Cu-HHTP[001]	532	$\sim7.60\times10^{5}$	RSA	[55]
Cu-HHTP[100]		$\sim0.84\times10^{5}$		
PT-PA	532	-1.83×10^{6}	SA	[73]
PB-PA		-1.69×10^{6}		
PT-BD		0.79×10^{6}	RSA	
PB-BD		0.73×10^{6}		
Cu-TMPc	800	1.1×10^{4}	RSA	[71]
Zn-TMPc		1.4×10^{5}		
SURMOFs	800	-9.29×10^{5}	SA	[72]
Carbon quantum dots	532	2.94×10^{4}	RSA	[74]
Carbon nanotube film	1300	1.23×10^{4}	SA	[75]
Single-wall carbon nanotubes	1080	-5×10^{2}	SA	[76]

References

[59] Smith, D. D.; Yoon, Y.; Boyd, R. W.; Campbell, J. K.; Baker, L. A.; Crooks, R. M.; George, M. A. Z-Scan Measurement of the Nonlinear Absorption of a Thin Gold Film. J. Appl. Phys. 1999, 86 (11), 6200–6205.
[60] Rotenberg, N.; Bristow, A. D.; Pfeiffer, M.; Betz, M.; Driel, van. Nonlinear Absorption in Au Films: Role of Thermal Effects. Phys. Rev. B. 2007, 75 (15).
[61] Sakho, E. hadji M.; Oluwafemi, O. S.; Sreekanth, P.; Philip, R.; Thomas, S.; Kalarikkal, N. Improved Nonlinear Optical and Optical Limiting Properties in Non-Covalent Functionalized Reduced Graphene Oxide/Silver Nanoparticle (NF-RGO/Ag-NPs) Hybrid. Opt. Mater. 2016, 58, 476–483.
[62] Salah, A.; Mansour, A.; Mohamed, M. B.; Azzouz, I. M.; Elnaby, S.; Badr, Y. Effects of Nanoparticles Size and Concentration and Laser Power on Nonlinear Optical Properties of Au and Au–CdSe Nanocrystals. Appl. Surf. Sci. 2015, 353, 112–117.
[63] Zhang, Y.; Wang, Y. Nonlinear Optical Properties of Metal Nanoparticles: A Review. RSC Adv. 2017, 7 (71), 45129–45144.
[64] An, C.; Feng, X.; Zhao, N.; Liu, P.; Wang, T.; Lian, Z. Syntheses, Structures and Third-Order Nonlinear Optical Properties of Two-Dimensional Rhombohedral Grid Coordination Polymers: [Cd(Imz)3]2(BTC)·0.5H2O and [Cu4(H2O)2(Imz)8](BTC)2·7H2O(BTC = 1, 2, 4, 5-Benzenetetracarboxylate Anion, Imz = Imidazole). J. Clust. Sci. 2014, 26 (3), 889–900.
[65] Xu, Y.; Lu, Y.; Zuo, Y.; Xu, F.; Zuo, D. Z-Scan Measurements of Nonlinear Refraction and Absorption for Aluminum-Doped Zinc Oxide Thin Film. Appl. Opt. 2019, 58 (22), 6112–6112.
[66] Liu, Z.; Sun, J.; Yan, C.; Xie, Z.; Zhang, G.; Shao, X.; Zhang, D.; Zhou, S. Diketopyrrolopyrrole Based Donor–Acceptor π-Conjugated Copolymers with Near-Infrared Absorption for 532 and 1064 Nm Nonlinear Optical Materials. J. Mater. Chem. C. 2020, 8 (37), 12993–13000.
[67] Zhu, Z.-Y.; Wang, Z.; Li, Q.-H.; Ma, Z.-Z.; Wang, F.; Zhang, J. Porphyrin Metal–Organic Frameworks with Bilayer and Pillar-Layered Frameworks and Third-Order Nonlinear Optical Properties. Dalton Trans. 2023, 52 (14), 4309–4314.
[68] Zhang, Y.; Yan, L.; Li, Y.; Si, J.; Tan, W.; Hou, X. Nonlinear Optical Limiting Effect and Charge Transfer Dynamics in a Fe-Porphyrin Metal-Organic Framework. Opt. Mater. Express. 2023, 13 (2), 484.
[69] Li, D.-J.; Li, Q.-H.; Wang, Z.-R.; Ma, Z.-Z.; Gu, Z.-G.; Zhang, J. Interpenetrated Metal-Porphyrinic Framework for Enhanced Nonlinear Optical Limiting. J. Am. Chem. Soc. 2021, 143 (41), 17162–17169.
[70] Tian, Y.-B.; Li, Q.-H.; Wang, Z.; Gu, Z.-G.; Zhang, J. Coordination-Induced Symmetry Breaking on Metal-Porphyrinic Framework Thin Films for Enhanced Nonlinear Optical Limiting. Nano Lett. 2023, 23 (7), 3062–3069.
[71] Srivishnu, K. S.; Banerjee, D.; Ramya Athira Ramnagar; Rathod, J.; Lingamallu Giribabu; Venugopal Rao Soma. Optical, Electrochemical, Third-Order Nonlinear Optical Investigations of 3,4,5-Trimethoxy Phenyl Substituted Non-Aqueous Phthalocyanines. Front. Chem. 2021, 9.
[72] Gu, C.; Zhang, H.; You, P.; Zhang, Q.; Luo, G.; Shen, Q.; Wang, Z.; Hu, J. Giant and Multistage Nonlinear Optical Response in Porphyrin-Based Surface-Supported Metal–Organic Framework Nanofilms. Nano Lett. 2019, 19 (12), 9095–9101.
[73] M. Li, C. Gong, J. Du, D. Ding, D. Du, D. Wang, J. Jiang, T. Li, C. Zheng, Y. F. Yang, Y. She, J. Jia, Donor–Acceptor Covalent Organic Frameworks Films with Ultralow Band Gaps to Enhanced Third-Order Nonlinear Optical Properties, ACS Mater. Lett., 2023, 5, 694–703.

[74] P. Surendran, A. Lakshmanan, S. Sakthy Priya, K. Balakrishnan, P. Rameshkumar, K, Kannan, K. Mahalakshmi, V. Gayathri, G. Vinitha, Synthesis of fluorescent carbon quantum dots from Manihot esculenta waste peels for nonlinear optical and biological applications, Chemical Physics 2024, 8, 100515.

[75] V.V. Vanyukov, M.V. Shuba, A.G. Nasibulin, Y.P. Svirko, P.P. Kuzhir, G.M. Mikheev, Saturable absorption and nonlinear refraction in free-standing carbon nanotube film: Theory and experiment, Carbon 2022, 186, 509-519.

[76] D. V. Khudyakov, A. S. Lobach, V. A. Nadtochenko, Nonlinear optical absorption of single-wall carbon nanotubes in carboxymethylcellulose thin polymer film and its application as a saturable absorber for mode-locking in pulsed Nd:glass laser, Appl. Opt. 2009, 48, 1624-1627.

[77] Y. Miao and M. Tsapatsis, Electron Beam Patterning of Metal–Organic Frameworks, Chemistry of Materials, 2021, 33, 754–760.

[78] Y. Lu, X. Zhang, L. Zhao, H. Liu, M. Yan, X. Zhang, K. Mochizuki and S. Yang, Metal-organic framework template-guided electrochemical lithography on substrates for SERS sensing applications, Nat. Commun., 2023 ,14, 5860.

[79] J. Troyano, A. Carné-Sánchez and D. Maspoch, Programmable Self-Assembling 3D Architectures Generated by Patterning of Swellable MOF-Based Composite Films, Adv. Mater. 2019, 31, 1808235.

[80] O. Dalstein, E. Gkaniatsou, C. Sicard, O. Sel, H. Perrot, C. Serre, C. Boissière and M. Faustini, Evaporation-Directed Crack-Patterning of Metal–Organic Framework Colloidal Films and Their Application as Photonic Sensors, Angew. Chem. Int. Ed., 2017, 56, 14011–14015.